LiNbO₃-based integrated optical network analyser for vectorial structure characterisation of fibre Bragg gratings

S. Bhandare, D. Sandel, R. Noé, R. Ricken, H. Suche and W. Sohler

Abstract: A LiNbO₃-based integrated optical network analyser for polarisation-resolved long-itudinal structure characterisation of optical fibre Bragg gratings is reported. The frequency-dependent complete reflectance Jones matrix is measured by interferometry and transformed into the time-domain impulse response. From the impulse response matrix the vectorial grating structure is determined by inverse scattering. Local dichroic reflectivity and birefringence were derived from this data. Knowledge of the vectorial nature of refractive index modulation depth and phase should allow an improvement of the ultraviolet (UV) illumination process and an effective correction of phase mask errors by longitudinally selective UV light post-processing, in order to fabricate chirped and/or apodised gratings which require the highest fabrication accuracy.

1 Introduction

Fibre Bragg gratings [1] are key elements in the established fields of optical communication, optoelectronics and optical sensors. They are comparatively simple devices and in their most basic form consist of a periodic modulation of the index of refraction along the fibre core. There are various types of Bragg gratings that differ by application and hence by refractive index modulation. Of great interest are chirped gratings for dispersion compensation, which require the highest fabrication accuracy [2, 3]. For polarisation-insensitive operation, not only the desired refractive index modulation must be performed precisely but the grating must also be free from birefringence and dichroism. The fabrication process has, therefore, to be optimised in all these respects. To what extent the specific Bragg grating design and the actual fabricated device correspond to each other has to be checked by appropriate measurements. Acquired knowledge about the vectorial nature of refractive index modulation depth and phase should allow for a correction of aberrations from the desired structure by effectively correcting the phase mask errors by longitudin-ally selective UV light post-processing.

The common 'single-mode' optical fibres are in fact two-moded. The two propagating modes that the fibre supports are nearly degenerate and differ mainly by polarisation. Most optical components are sensitive to the state of polarisation and, therefore, a full account of its evolution is essential in optical network analysis. Noninterferometric techniques rely on modulation. In fact, any direct detection experiment with analogue intensity modulation and an electrical network analyser connected to the transmitter input and the receiver output yields an electrical transfer function from which magnitude and delay of the optical transfer function are obtained. This scheme can be expanded to include different polarisations [4]. The phase of the optical transfer function is only accessible by integrating the group delay over frequency. But this scheme limits the accuracy and does not allow the determination of the correct phase relationship between transfer functions obtained from different polarisations.

Optical network analysis is a direct analogy of electrical network analysis; since the optical fields transfer functions are measured directly. It is suitable for characterising optical components, such as Bragg gratings, during and after fabrication. An interferometric technique with fixed polar-isations is the simplest one and is a one-port form of optical network analysis. Low-coherence interferometry [5] directly yields the impulse response of a device with $\sim 100\,\mu m$ spatial resolution. However, optical coherence domain interferometry [6], which is being used in this work, delivers the frequency-dependent complex reflection factors or transmission factors from which the impulse response is calculated. The laser tuning range limits spatial resolution, but large grating lengths may be investigated due to the high coherence of a single-mode laser. The impulse response allows us to determine the longitudinal structure of an isotropic grating [7] and, hence, the depth, or the magnitude and the phase, of the refractive index modulation using inverse scattering.

2 Calculation of refractive index matrix

A refractive index matrix of a uniform Bragg grating formed within the core of an optical fibre with an average refractive index of n_0 is written as

$$\boldsymbol{n}(z) = n_0 + \boldsymbol{\beta}(z)$$
$$+ \operatorname{Re}\left(\frac{1}{2}\begin{bmatrix} \Delta n_{pp11}(z) & \Delta n_{pp12}(z) \\ \Delta n_{pp12}^*(z) & \Delta n_{pp22}(z) \end{bmatrix} e^{j\left(\frac{2\pi z}{\Lambda} + \Phi(z)\right)}\right) \quad (1)$$

S. Bhandare, D. Sandel and R. Noé are with Optical Communication and High Frequency Engineering, University of Paderborn, Warburger Str. 100, Pader-born 33098, Germany

R. Ricken, H. Suche and W. Sohler are with Applied Physics, University of Paderborn, Warburger Str. 100, Paderborn 33098, Germany

where Δn_{pp} is the peak-to-peak refractive index modulation, $\beta(z)$ is the birefringence, Λ is the index modulation period and z is the distance along the fiber longitudinal axis. The coupling matrix between forward and backward propagating modes is

$$\boldsymbol{\kappa}(z) = \frac{j\pi}{2\lambda_{\mathrm{B}}} \begin{bmatrix} \Delta n_{pp11}(z) & \Delta n_{pp12}(z) \\ \Delta n_{pp11}^*(z) & \Delta n_{pp22}(z) \end{bmatrix} e^{j\Phi(z)}$$

$$= \boldsymbol{E}_\kappa \boldsymbol{\Lambda}_\kappa \boldsymbol{E}_\kappa^+ \qquad (2)$$

where λ_{B} is the Bragg wavelength with

$$\boldsymbol{\Lambda}_\kappa = \begin{bmatrix} \kappa_1 & 0 \\ 0 & \kappa_2 \end{bmatrix} \arg(\kappa_1) = \arg(\kappa_2) \qquad (3)$$

representing grating reflectivity. A Hermitian matrix with peak-to-peak refractive index modulation amplitudes $\Delta n_{ppij}(z)$ is preceded by a phasor containing the mean reflection or grating phase $\Phi(z)$. Diagonalisation of (2) yields two complex eigenvalues κ_1 and κ_2 with equal phase angles (three unknowns) and complex orthogonal eigenmodes (two unknowns), which form a unitary eigenvector matrix $\boldsymbol{E}_\kappa$. The birefringence matrix

$$\boldsymbol{\beta}(z) = \frac{\pi}{2\lambda_{\mathrm{B}}} \begin{bmatrix} \Delta n_{11}(z) & \Delta n_{12}(z) \\ \Delta n_{11}^*(z) & -\Delta n_{11}(z) \end{bmatrix} = \boldsymbol{E}_\beta \boldsymbol{\Lambda}_\beta \boldsymbol{E}_\beta^+ \qquad (4)$$

represents a lossless retarder with refractive index difference $\Delta n_{ij}(z)$. This special Hermitian matrix has real eigenvalues $\pm\beta$ (one unknown) and complex orthogonal eigenmodes (two unknowns), which form a unitary eigenvector matrix $\boldsymbol{E}_\beta$.

$\boldsymbol{\kappa}$ and $\boldsymbol{\beta}$ vary slowly with respect to positional co-ordinate z. The eight real unknowns in $\boldsymbol{\kappa}$ and $\boldsymbol{\beta}$ are balanced by the four complex elements of the 2×2 Jones reflectance matrix

$$\boldsymbol{\rho}(f) = \begin{bmatrix} \rho_{r\|,t\|}(f) & \rho_{r\|,t\perp}(f) \\ \rho_{r\perp,t\|}(f) & \rho_{r\perp,t\perp}(f) \end{bmatrix} \qquad (5)$$

of the grating. Subscripts $\|$ and $\perp$ refer to pairs of orthogonal polarisation, both at the input of the device under test and reference analysed at its output. For grating structure calculation, the matrix impulse response

$$\boldsymbol{U}(0,t) = \begin{bmatrix} u_{r\|,t\|}(0,t) & u_{r\|,t\perp}(0,t) \\ u_{r\perp,t\|}(0,t) & u_{r\perp,t\perp}(0,t) \end{bmatrix} \qquad (6)$$

is calculated by inverse Fourier transform of each of the reflectances

$$u_{r_i,t_j}(0,t) = F^{-1}(\rho_{r_i,t_j}(f)) \qquad (7)$$

$\boldsymbol{U}(0,t)$ can be indeed considered as a response to $\boldsymbol{D}(0,t) = \boldsymbol{I}\delta(t)$, a Dirac impulse unity matrix.

More generally, propagation of the wave in time t and one-dimensional space co-ordinate z is governed by the coupled differential equations

$$\left(\frac{\partial}{\partial z} + \frac{n_o}{c} \frac{\partial}{\partial t} \right) \boldsymbol{D}(z,t) = -j\boldsymbol{\beta}(z)\boldsymbol{D}(z,t) + \boldsymbol{\kappa}^+(z)\boldsymbol{U}(z,t)$$

$$\left(\frac{\partial}{\partial z} - \frac{n_o}{c} \frac{\partial}{\partial t} \right) \boldsymbol{U}(z,t) = +j\boldsymbol{\beta}(z)\boldsymbol{U}(z,t) + \boldsymbol{\kappa}(z)\boldsymbol{D}(z,t) \qquad (8)$$

where $\boldsymbol{D}$ is the electric field matrix of the forward-propagating waves and $\boldsymbol{U}$ is the electric field matrix of the backward-propagating waves. In order to calculate $\boldsymbol{\kappa}(z)$ and $\boldsymbol{\beta}(z)$, the above coupled differential equations (8) are discretised using the position step Δz and a corresponding time step $\Delta t = n_0/c\Delta z$. A pair of discrete equations

$$\boldsymbol{D}_{\mu,\nu} = \boldsymbol{\tau}_{\mu-1}^{-1}(\boldsymbol{b}_{\mu-1}\boldsymbol{D}_{\mu-1,\nu-1} - \boldsymbol{k}_{\mu-1}^+ \boldsymbol{b}_{\mu-1}^{-1} \boldsymbol{U}_{\mu-1,\nu-1})$$

$$\boldsymbol{U}_{\mu,\nu} = \boldsymbol{\tau}_{\mu-1}^{-1}(\boldsymbol{b}_{\mu-1}^{-1}\boldsymbol{U}_{\mu-1,\nu+1} + \boldsymbol{k}_{\mu-1}\boldsymbol{b}_{\mu-1}\boldsymbol{D}_{\mu-1,\nu+1}) \qquad (9)$$

is derived from the piecewise solution of (8) where $\boldsymbol{k} = \boldsymbol{\kappa}\Delta z$ and $\boldsymbol{b} = \exp(-j\boldsymbol{\beta}\Delta z)$ of position step Δz. Transmission matrix $\boldsymbol{\tau}$ must satisfy the lossless relation

$$\boldsymbol{\tau}\boldsymbol{\tau}^+ + \boldsymbol{k}\boldsymbol{k}^+ = \boldsymbol{I} \qquad (10)$$

Figure 1 shows the wave propagation and solution sequence in a grid of time t and one-dimensional space co-ordinate z. Solution starts from the knowledge of the incidence of the unity matrix $\boldsymbol{D}_{0,0}$ (the only nonzero component of a discretised $\boldsymbol{D}(0,t) = \boldsymbol{I}\delta(t)$) and the measured impulse response matrix $\boldsymbol{U}_{0,\nu}$ (discretised $\boldsymbol{U}(0,t)$). Waves $\boldsymbol{D}_{\mu,\nu}$ and $\boldsymbol{U}_{\mu,\nu}$ and, as yet unknowns, $\boldsymbol{k}$ and $\boldsymbol{b}$ are calculated in a sequence given by arrows. For the calculation of $\boldsymbol{k}_m$ and $\boldsymbol{b}_m$, all $\boldsymbol{k}_\mu$, $\boldsymbol{b}_\mu$ and $\boldsymbol{\tau}_\mu$ with $0 < \mu < \mathrm{m}$ must be known. This is automatically the case if one starts with $m = 1$. Each solution step requires the difference equations to be successively solved for $\mu = 1 \cdots m$, $\nu = 2m - \mu$. $\boldsymbol{D}_{m,m}$ and $\boldsymbol{U}_{m,m}$ are obtained as intermediate results and the matrix quotient

$$\boldsymbol{Q}_m = -\boldsymbol{U}_{m,m}\boldsymbol{D}_{m,m}^{-1} = \boldsymbol{b}_m \boldsymbol{k}_m \boldsymbol{b}_m \qquad (11)$$

has to be decomposed in a such way that

$$\boldsymbol{Q}^+\boldsymbol{Q} = (\boldsymbol{b}\boldsymbol{k}\boldsymbol{b})^+ \boldsymbol{b}\boldsymbol{k}\boldsymbol{b} = \boldsymbol{b}^+ \boldsymbol{E}_\kappa \boldsymbol{\Lambda}_\kappa^+ \boldsymbol{\Lambda}_\kappa \boldsymbol{E}_\kappa^+ \boldsymbol{b} \qquad (12)$$

which delivers $|\kappa_1|$ and $|\kappa_2|$ as the square root of its eigenvalues. The missing argument is

$$\arg(k_1) = \arg(k_2)$$

$$= \frac{1}{2}\arg(\det(\boldsymbol{k})) \text{ or } \frac{1}{2}\arg(\det(\boldsymbol{k})) + \pi \qquad (13)$$

Second eigenvector matrix $\boldsymbol{E}_\kappa^+ \boldsymbol{\beta}$ allows us the calculation of

$$\boldsymbol{b}\boldsymbol{E}_\kappa = \boldsymbol{Q}(\boldsymbol{E}_\kappa^+ \boldsymbol{b})^+ \boldsymbol{\Lambda}_\kappa^{-1} \qquad (14)$$

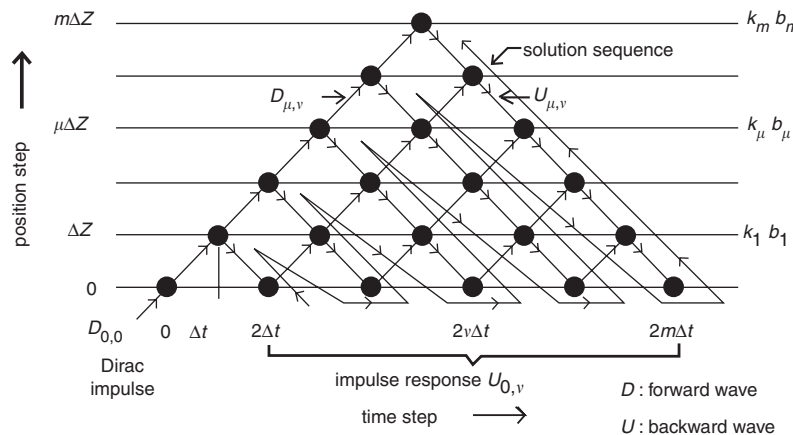**Fig. 1** *Wave propagation and solution sequence for inverse scattering algorithm*

which allows us to calculate

$$b = \sqrt{(bE_\kappa)(E_\kappa^+ b)} \qquad (15)$$

Expecting a small retardation due to b within Δz, the ambiguities of (13) and (15) can be settled so that the argument of eigenvalues of b are closest to zero. Once locally varying $\kappa = k/\Delta z$ and $\beta = j\ln(b)/\Delta z$ are calculated then the local peak-to-peak refractive index modulation $\Delta n_{ppij}(z)$, grating phase $\Phi(z)$ and their differences, $\Delta n_{ij}(z)$ (birefringence), are calculated.

3 Measurement setup

The measurement setup of our integrated optical network analyser consists of optics and electronics. A 10 dB coupler is connected to a tunable laser in order to monitor the laser power. A 3 dB coupler splits the remaining power between two Mach–Zehnder interferometers (MZI). The first MZI is a reference interferometer whose optical path length is adjusted to 0.5 m and acts as a high-resolution wavelength meter for frequency correction. The second MZI is a hybrid fibre and integrated optic interferometer and is used for measurement. It consists of an integrated optical network analyser (ONWA) chip, based on *X*-cut, *Z*-propagation LiNbO$_3$, and a 3×3 fibre coupler. Reflecting devices under test are connected to this MZI by means of an additional coupler. A 3×3 fibre coupler with three photodiodes at its outputs is used because it allows a more accurate phase measurement than a standard 2×2 coupler [8]. Real and imaginary parts of either the frequency-dependent complex reflection coefficient or the complex transmission coefficient of the DUT are calculated from two linear combinations of a respective three-phase photocurrent, obtained from these three photodiodes connected to the outputs of the respective 3×3 coupler. Optical isolators are used to avoid any stray reflections from the photodiodes back into the measurement MZI. The electronic hardware includes an eight-channel data acquisition system and a 16-channel digital-to-analogue converter developed in-house. It consists of gain programmable transimpedance amplifiers, inverting voltage amplifiers for additional gain, integrators and analogue-to-digital (A/D)

converter for each channel. A 16-channel digital-to-analog (D/A) conversion unit has built-in high-voltage amplifiers having an output voltage swing of ± 70 V, and these are used to drive phase shifter and TE–TM mode converter electrodes. A simple proportional-integral temperature controller is used to keep the LiNbO$_3$ chip temperature constant. A DFB laser diode was chosen as a tuneable laser source, and the ~ 50 GHz electrical tuning range is used to keep the measurement time short. It is interfaced to the computer system through a programmable constant current source. The advantage of this technique is that one can have high-resolution wavelength steps, even within the linewidth of the single-mode DFB laser diode. At the same time it allows us to do high-speed measurements, the major advantage of electronic tuning. Figure 2 shows the measurement setup.

4 Design and development of LiNbO$_3$ chip

The LiNbO$_3$ chip is based on *X*-cut, *Z*-propagation and is a key component in the measurement setup. A single-mode optical power splitter (*Y*-branch circuit) was realised in LiNbO$_3$ using standard Ti in-diffused optical waveguide technology. The chip uses a set of three metal-clad polarisers (TE-pass), a set of two phase shifters and a TE–TM mode converter on each branch of the power splitter. The integrated optic phase shifter allows digital phase shifting and performs an AC rather than a DC measurement in order to increase sensitivity. On-chip TE-pass polarisers maintain a reference polarisation and ensure that only phase-modulated light with a single polarisation enters the mode converter section. The integrated optic TE–TM mode converters act as calibrated polarisation transformers and are used to generate the required polarisations for vectorial measurement. Initially, near-*Z*-axis propagation was chosen for the device fabrication in order to compensate for the modal birefringence of the on-chip TE–TM mode converter sections. In this compensation process, one always ends up with an undesired imaginary coupling coefficient between the two orthogonally polarised modes. This not only makes the TE–TM mode converter nonideal, but also affects the
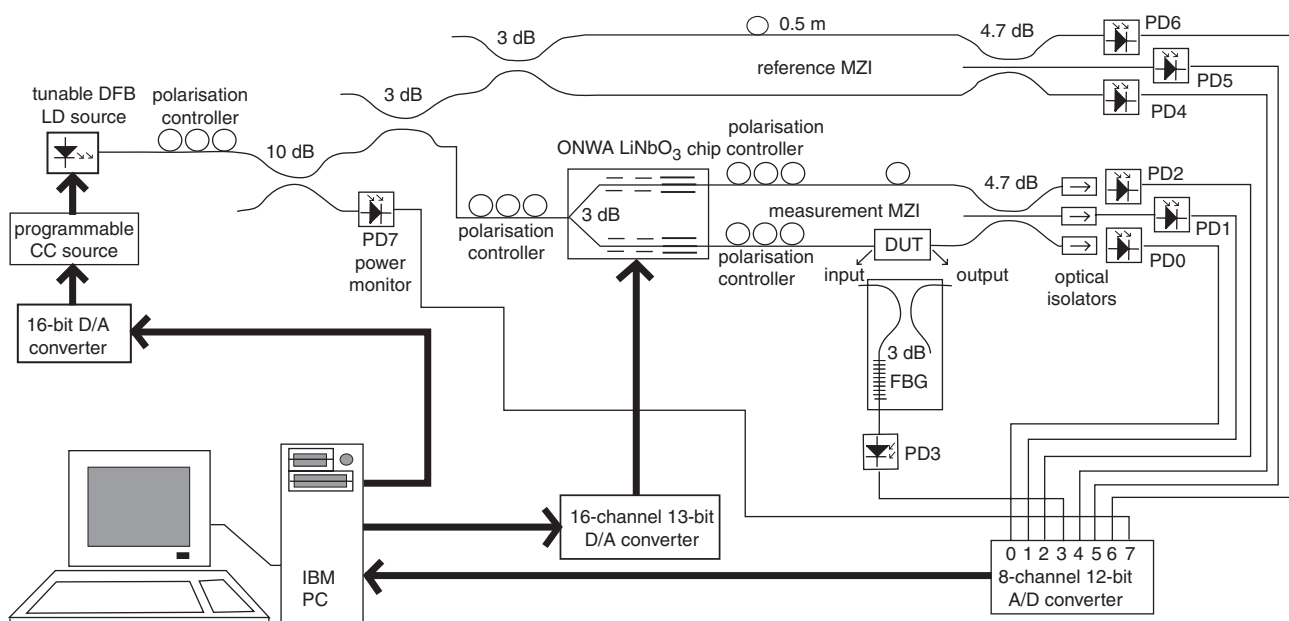

Fig. 2 *Measurement setup of integrated optical network analyser*

performance of on-chip polarisers. Macroscopically it behaves like a reciprocal circular birefringence. It degrades the polarisation extinction ratio (PER) of the polarisers because the TM-polarised mode is regenerated in the waveguide after the polarisers [9]. Therefore, principal-axis propagation was used in the next generation of these chips.

The yttrium oxide based metal-clad polarisers were optimised to give an extinction ratio of nearly 30 dB for 3-mm long polarisers with 27-nm thick Y_2O_3 and 500-nm thick aluminium after several trials. The voltage V_π of the phase shifters was characterised using a Fabry–Perot technique. Figure 3a shows the characteristic response of the phase shifter. $V_\pi = 40$ V holds for these 15-mm long devices. The voltage-length product (60 V-cm) was found to be constant for phase shifters. The TE–TM mode converters were characterised for their conversion efficiency. This was found to be >99%. The voltage required for full TE–TM mode conversion was 10 V and the bias voltages required for the compensation of modal birefringence were ± 38 V. Figure 3b shows experimentally obtained TE–TM mode converter switching curves. This chip was fibre-pigtailed with slanted endfaces in order to improve input/output optical return loss (Fig. 4).
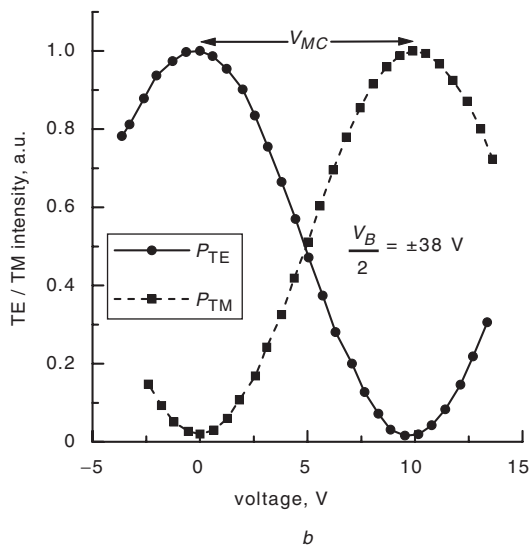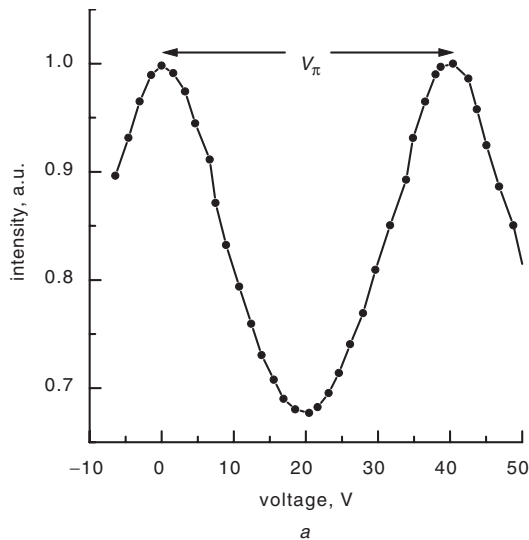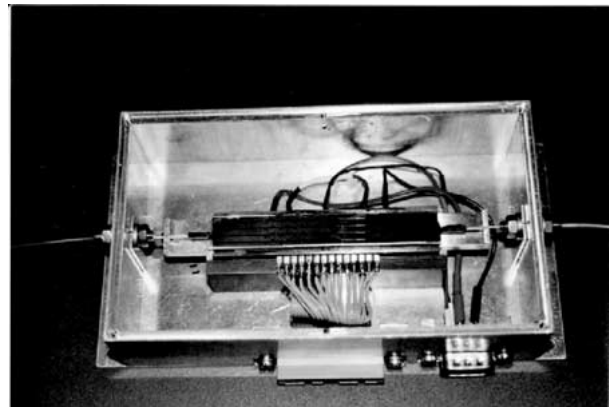

Fig. 4 *Photograph of fibre-pigtailed and packaged LiNbO₃-based integrated optical network analyser chip*

5 Fibre Bragg grating characterisation

A uniform fibre Bragg grating at 1548 nm having reflectivity >95 % and a 0. 20 nm bandwidth was chosen as a device under test for longitudinal structure characterisation. For the measurement of the complex scattering parameters (reflection factors $\rho(f)$) the optical frequency was scanned
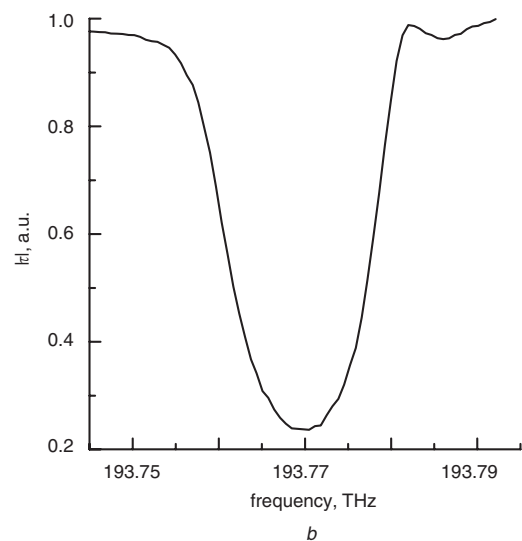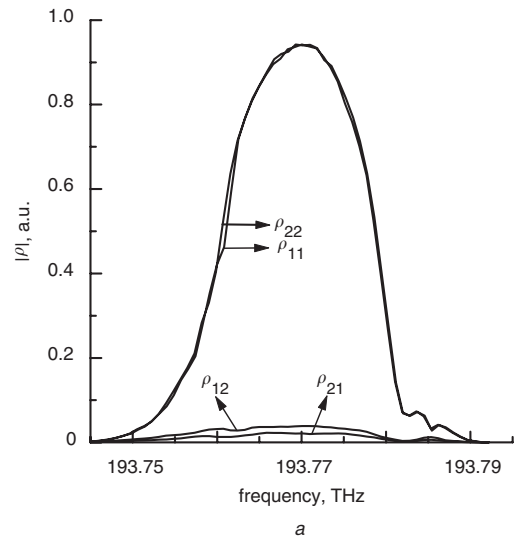

Fig. 3 *Phase shifter and TE–TM mode converter responses*
a Phase shifter
b TE–TM mode converter

Fig. 5 *Scattering parameters (a) and scalar transmission coefficient $|\tau(f)|$ (b) in forward direction as a function of optical frequency*

symmetrically over $\sim 50\,\mathrm{GHz}$ optical bandwidth with the Bragg wavelength ($\lambda_B = 1548\,\mathrm{nm}$) being at the scan centre. The frequency resolution was chosen as $\sim 25\,\mathrm{MHz}$. The DFB laser linewidth was $\sim 1\,\mathrm{MHz}$. Algorithms were developed in 'C' for the automated measurement, data acquisition, preprocessing of reflectometric data, inverse Fourier transform and inverse scattering for scalar as well as vectorial measurements. Reflectometric data was analysed using this software to reveal the vectorial structure of the uniform Bragg grating.

A cleaved bare fibre has a small but frequency and polarisation independent reflectivity and is used for calibrating the measurement setup. Scattering parameters, impulse response matrix elements and derived grating structure (Jones matrix elements) were identical when like measurements were performed from both sides of the grating (see Figs. 5 and 6). This validates the function of the ONWA. The calculated birefringence (not shown) of this commercial grating was negligible.
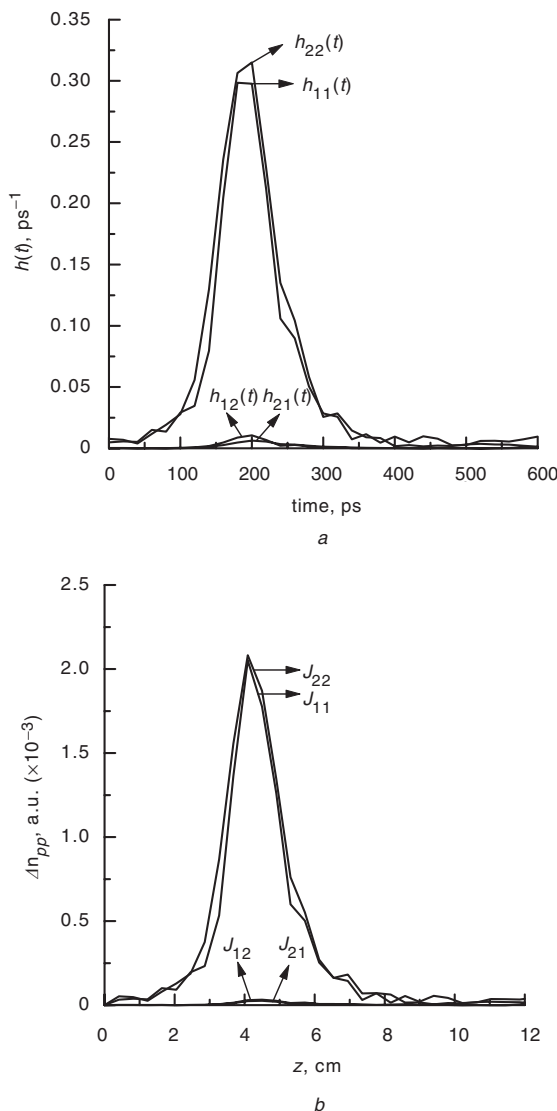

Fig. 6 *Impulse response matrix elements (a) and longitudinal grating structure (b) in forward direction*

6 Summary

An advanced optical network analyser using an integrated-optic lithium niobate chip for vectorial structure characterisation of optical fibre Bragg gratings is reported. On-chip TE-pass polarisers maintain reference polarisations and ensure that only phase-modulated light with a single polarisation enters the mode converter sections. The TE–TM mode converters act as calibrated polarisation transformers and are used to generate the required polarisations for vectorial measurement. The ONWA function for vectorial measurements was validated using a commercial Bragg grating. Local dichroic reflectivity and birefringence was obtained from this data. The isotropic grating structure has been obtained in less time with high accuracy. One frequency scan takes a few seconds, in contrast to the previous setup where it took 15 minutes. One main reason for this improvement is that the electro-optic polarisation transformers replaced the previously used fibre squeezers. Also, the optical phase shifters allowed digital phase shifting to perform an AC rather than a DC measurement for increased accuracy and sensitivity. Results may be used to optimise refractive index modulation depth, phase mask pitch and the UV illumination process.

7 Acknowledgments

8 References

1 Hill, K.O., Malo, B., Bilodeau, F., Johnson, D.C., and Albert, J.: 'Bragg gratings fabricated in monomode photosensitive optical fibre by UV exposure through phase mask', *Appl. Phys. Lett.*, 1993, **62**, pp. 1035–1037
2 Cole, M.J., Geiger, H., Laming, R.I., Set, S.Y., Zervas, M.N., Loh, W.H., and Gusmeroli, V.: 'Continuously chirped broadband dispersion compensating fiber gratings in a 10 Gbit/s 110 km standard fibre link'. Proc. 22nd ECOC, Oslo, Norway, September 1996, Vol. 5, ThB. 3.5, pp. 19–22
3 Ouellette, F., Krug, P.A., Stephens, T., Dhosi, G., and Eggeleton, B.: 'Broadband and WDM dispersion compensation using chirped sampled fibre Bragg gratings', *Electron. Lett.*, 1995, **31**, pp. 899–901
4 Sano, K., Kudou, T., and Ozeki, T.: 'Simultaneous measurement of group delay time dispersion and polarization mode dispersion'. Proc. 22nd ECOC, Oslo, Norway, September 1996, TuP.09, pp. 253–256
5 Lambelet, P., Fonjallaz, P.Y., Limberger, H.G., Salathé, R.P., Zimmer, C., and Gligen, H.H.: 'Bragg grating characterization by optical low coherence reflectometry', *IEEE Photonics Technol. Lett.*, 1993, **5**, pp. 565–567
6 Sandel, D., Noé, R., Heise, G., and Borchert, B.: 'Optical network analysis and longitudinal structure characterization of fiber Bragg gratings', *J. Lightwave Technol.*, 1998, **16**, pp. 2435–2442
7 Brinkmeyer, E.: 'Simple algorithm for reconstructing fiber gratings from reflectometric data', *Opt. Lett.*, 1995, **20**, pp. 810–812
8 Priest, R.G.: 'Analysis of fibre interferometers utilizing 3×3 fibre couplers', *IEEE J. Quantum Electron.*, 1982, **QE-18**, pp. 1601–1603
9 Bhandare, S., Noé, R., and Sandel, D.: 'Origin of reciprocal circular birefringence observed in *X*-cut, *Z*-propagation LiNbO$_3$ polarization transformers', *Appl. Phys. B, Lasers Opt.*, 2001, **73**, pp. 549–553